

Strong Optical–Optical Avoided Crossings Suppress Thermal Conductivity in Ga-Substituted TlInTe₂

Sayan Paul¹ and Swapan K. Pati^{1,*}

¹*Theoretical Sciences Unit, School of Advanced Materials (SAMat),
Jawaharlal Nehru Centre for Advanced Scientific Research, Bangalore 560064, India*

(Dated: June 5, 2026)

In crystalline solids, avoided crossing between acoustic and optical phonons is widely recognized as an effective mechanism for suppressing lattice thermal conductivity (κ_l). However, the role of avoided crossings among optical phonons remains largely unexplored due to their weak contribution to heat transport. Here, using first-principles calculations combined with the linearized Wigner transport equation (LWTE), we demonstrate that optical–optical avoided crossings can effectively reduce (κ_l) in TlIn_{0.5}Ga_{0.5}Te₂. Pristine TlInTe₂ exhibits strong optical phonon-dominated heat transport, where optical phonons contribute nearly 63% of κ_l . The phonon dispersion of TlInTe₂ shows several crossing points in the optical region, which evolve into avoided crossings after 50% Ga substitution. Irreducible representation analysis reveals that the crossing phonon branches in TlInTe₂ belong to different symmetry representations, whereas the corresponding branches in TlIn_{0.5}Ga_{0.5}Te₂ possess the same symmetry representation, which enables phonon modes to couple and results in gap opening at the crossing points. These avoided crossings significantly suppress the optical phonon group velocity, thereby reducing the optical phonon contribution from 63% to 44% and lowering κ_l from 0.568 to 0.482 Wm⁻¹K⁻¹ at 300 K. Mode-averaged transport analysis further confirms that the suppression of κ_l is primarily governed by reduced phonon group velocity (v_g), while enhanced anharmonic scattering provides an additional secondary contribution. Our results establish symmetry-modified optical–optical avoided crossing as an effective route to suppress optical phonon transport and reduce κ_l in systems where optical phonons significantly contribute to heat transport.

I. INTRODUCTION

Materials exhibiting intrinsically low lattice thermal conductivity (κ_l) are of significant interest for their application in thermoelectrics,[1–3] thermal barrier coatings,[4] heat management, [5] and photovoltaics, [6] etc. Thus, understanding and engineering phonon dynamics and phonon-mediated thermal transport to achieve reduced κ_l are extremely crucial. Over the years, various intrinsic and extrinsic approaches have been explored to tailor lattice thermal transport. Intrinsic strategies, such as bonding heterogeneity,[7] rattler-like atoms,[8, 9] lattice instability associated with Pauling’s 3rd rule,[10, 11] liquid-like sublattice,[12] ferroelectric instability,[13] antibonding states below the Fermi level,[14] etc. are widely used to design novel low κ_l materials. On the other hand, extrinsic approaches, including all-scale hierarchical phonon engineering,[15, 16] entropy-driven alloying,[17, 18] defect engineering,[19] etc. are employed to modulate thermal transport of a material.

Within the phonon gas model, the lattice thermal conductivity of crystalline solids is expressed as $\kappa_l = \frac{1}{3}C_V v_g l$, where C_V is the phonon specific heat, v_g is the group velocity, and l is the phonon mean free path.[20] So, the acoustic phonon modes, which are typically highly dispersive and possess large v_g and long l , dominate in heat transport. In contrast, optical phonons are generally less dispersive, leading to lower v_g and a short mean free path. Therefore, their contribution to heat transport is significantly less com-

pared to acoustic phonons. Thus, controlling the dispersion of acoustic phonons is one of the primary strategies to suppress the κ_l . [21, 22] In several halide and chalcogenide-based compounds, such as Cs₃Bi₂I₆Cl₃, [23, 24] KCu₅Se₃, [25] TlCuSe, [26] and Tl₂AgI₃ [11] etc., the presence of low-frequency localized optical phonon modes has been shown to strongly scatter heat-carrying acoustic phonons, which reduces κ_l . In cage-like materials such as skutterudites and clathrates, the loosely bound guest atoms move independently from the host matrix, which is referred as “rattling” motion or Einstein-like motion. [27–29] These rattling vibrations give rise to low-frequency, localized optical phonon modes that lie in close proximity to acoustic branches. [30] Inelastic neutron scattering experiments have shown that these modes hybridize with acoustic phonons, leading to avoided crossings that suppress the dispersion of acoustic branches, reduce their v_g and effectively suppress κ_l . [8]

Avoided crossing in phonon arises when two phonon modes of same symmetry interact and hybridize with each other, so they do not intersect. [8] Instead of crossing, they repel each other and a characteristic gap opening is observed at the crossing point, which reduces their group velocity (FIG. 1). Avoided crossings between acoustic and optical phonons have been extensively studied as an effective strategy to reduce κ_l in many compounds. [31, 32] However, avoided crossing between optical phonons has received very little attention due to the small contribution of optical phonons to κ_l . Interestingly, recent studies have revealed that optical phonons can contribute significantly to κ_l in certain systems. For example, in SnSe [33] and BaSnS₂ [34] crystals, ~60% and ~68% of total κ_l is contributed by the optical phonons, respectively. In such cases, engineering the dispersion of

* pati@jncasr.ac.in

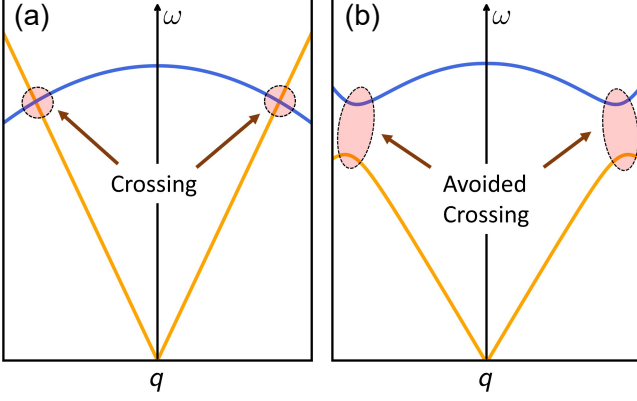


FIG. 1. Schematic illustration of (a) phonon branch crossing and (b) avoided crossing arising from mode coupling. In (a), two non-interacting phonon modes intersect due to symmetry incompatibility. In (b), interaction between modes with compatible symmetry leads to hybridization, resulting in band repulsion, and a finite frequency gap at the crossing point leads to the avoided crossing region.

optical phonons provides an alternative pathway to modulate thermal transport.

In this work, we demonstrate that chemical substitution modifies the symmetry characteristics of optical phonon modes, leading to avoided crossings among optical phonons and reducing the overall κ_l . We choose a well-studied ternary chalcogenide compound TlInTe_2 from the ABX_2 ($A = \text{In}^+, \text{Tl}^+$, $B = \text{Ga}^{3+}, \text{In}^{3+}, \text{Tl}^{3+}$, $X = \text{Se}^{2-}, \text{Te}^{21}$) family, which shows ultra-low κ_l due to the presence of rattler cation at A site.[35, 36] We observe several crossings in the phonon dispersion at the optical phonon region of pristine TlInTe_2 . Due to the high dispersion of these modes, we show that optical phonons contribute $\sim 63\%$ to heat transport, as evidenced by cumulative κ_l analysis. Upon 50% Ga substitution at the In site, the crossing points evolve into avoided crossings, resulting in pronounced flattening of the optical branches and a corresponding reduction in v_g . Consequently, optical phonon contribution to κ_l is reduced to $\sim 44\%$, which suppress the overall κ_l of $\text{TlIn}_{0.5}\text{Ga}_{0.5}\text{Te}_2$ to $0.482 \text{ Wm}^{-1}\text{K}^{-1}$ from $0.568 \text{ Wm}^{-1}\text{K}^{-1}$ of TlInTe_2 . Thus, our results establish a distinct mechanism of modulating κ_l by tuning of the optical phonons effectively.

II. COMPUTATIONAL METHODOLOGY

We carried out first-principles DFT calculations in the Vienna Ab initio Simulation Package (VASP)[37, 38] using the projected augmented wave (PAW)[39, 40] pseudopotentials of Tl ($5d^{10} 6s^2, 6p^1$), In ($4d^{10} 5s^2, 5p^1$), Ga ($3d^{10} 4s^2, 4p^1$) and Te ($5s^2, 5p^4$). The Perdew, Burke and Ernzerhof functional for solids (PBEsol)[41, 42] within the generalized gradient approximation (GGA) is used for describing the exchange-correlation energies. The electronic wavefunctions were expanded using a plane wave basis set with a 650 eV kinetic energy cutoff, and a Γ -centered $12 \times 12 \times 12$ mesh was employed for the Brillouin

loun zone sampling. The threshold criteria for energy and Hellmann-Feynman force convergence were set to 10^{-8} eV and 10^{-4} eV/Å, respectively.

The harmonic phonon dispersion was calculated using finite displacement method as implemented in the Phonopy package.[43, 44] We took a $3 \times 3 \times 3$ supercell (216 atoms) of the primitive unit cell (8 atoms) to generate the symmetry-inequivalent displaced structures, from which the dynamical matrix and harmonic second-order interatomic force constants (IFCs) were constructed via static DFT calculations.

To obtain the phonon relaxation time (τ) and anharmonic phonon properties, we constructed 3rd order IFC matrix from the displaced configuration generated from a $2 \times 2 \times 2$ supercell (64 atoms) using the Phono3py package.[43–45] Then, the κ_l and related anharmonic transport properties were evaluated by solving the linearized Wigner transport equation (LWTE),[46, 47] where κ_l is expressed as

$$\kappa_l^{\alpha\beta} = \kappa_p^{\alpha\beta} + \kappa_c^{\alpha\beta}. \quad (1)$$

Here, κ_p and κ_c represent the population (particle-like) and coherence (wave-like) contributions to κ_l , respectively. In κ_p mechanism heat is transported by the diagonal elements of the heat flux operator, which is same as the Boltzmann transport equation (BTE). κ_p is calculated by the direct solution of the BTE using the equation[48]

$$\kappa_p^{\alpha\beta} = \frac{\hbar^2}{4k_B T^2 N V_0} \sum_{\lambda\lambda'} \frac{\omega_\lambda v^\alpha(\lambda)}{\sinh\left(\frac{\hbar\omega_\lambda}{2k_B T}\right)} \frac{\omega_{\lambda'} v^\beta(\lambda')}{\sinh\left(\frac{\hbar\omega_{\lambda'}}{2k_B T}\right)} (\Omega^{-1})_{\lambda\lambda'}, \quad (2)$$

where Ω^{-1} denotes the Moore-Penrose inverse of the collision matrix Ω . The collision matrix is

$$\Omega_{\lambda\lambda'} = \delta_{\lambda\lambda'} \frac{1}{\tau_\lambda} + \frac{\pi}{\hbar^2} \sum_{\lambda''} |\Phi_{\lambda\lambda'\lambda''}|^2 \frac{1}{\sinh\left(\frac{\hbar\omega_{\lambda''}}{2k_B T}\right)} \times [\delta(\omega_\lambda - \omega_{\lambda'} - \omega_{\lambda''}) + \delta(\omega_\lambda + \omega_{\lambda'} - \omega_{\lambda''}) + \delta(\omega_\lambda - \omega_{\lambda'} + \omega_{\lambda''})]. \quad (3)$$

Here, k_B is the Boltzmann constant, ω_λ is the frequency of the phonon of mode λ , $v^\alpha(\lambda)$ is the velocity of λ phonon mode in α direction, T is temperature, $\Phi_{\lambda\lambda'\lambda''}$ is 3rd order IFC and τ_λ is phonon relaxation time. The equation is solved with a $12 \times 12 \times 12$ q -point mesh employing 2nd and 3rd order IFCs. The convergence of κ_l with q -mesh is shown in FIG. S2, Supplemental Material. Conversely, the coherence term κ_c originates from the off-diagonal elements of the heat flux operator, which captures wavelike heat transport arising from coupling between quasi-degenerate phonon modes. This mechanism is analogous to Allen-Feldmann theory for disordered solids.[49, 50] In the LWTE formalism κ_c is calculated using the equation[46, 47]

$$\kappa_c^{\alpha\beta} = \frac{\hbar^2}{k_B T^2} \frac{1}{\mathcal{V} N_c} \sum_{\mathbf{q}} \sum_{s \neq s'} \frac{\omega(\mathbf{q})_s + \omega(\mathbf{q})_{s'}}{2} v^\alpha(\mathbf{q})_{s,s'} v^\beta(\mathbf{q})_{s',s} \times \frac{\omega(\mathbf{q})_s \bar{N}^T(\mathbf{q})_s [\bar{N}^T(\mathbf{q})_s + 1] + \omega(\mathbf{q})_{s'} \bar{N}^T(\mathbf{q})_{s'} [\bar{N}^T(\mathbf{q})_{s'} + 1]}{4[\omega(\mathbf{q})_{s'} - \omega(\mathbf{q})_s]^2 + [\Gamma(\mathbf{q})_s + \Gamma(\mathbf{q})_{s'}]^2} \times [\Gamma(\mathbf{q})_s + \Gamma(\mathbf{q})_{s'}] \quad (4)$$

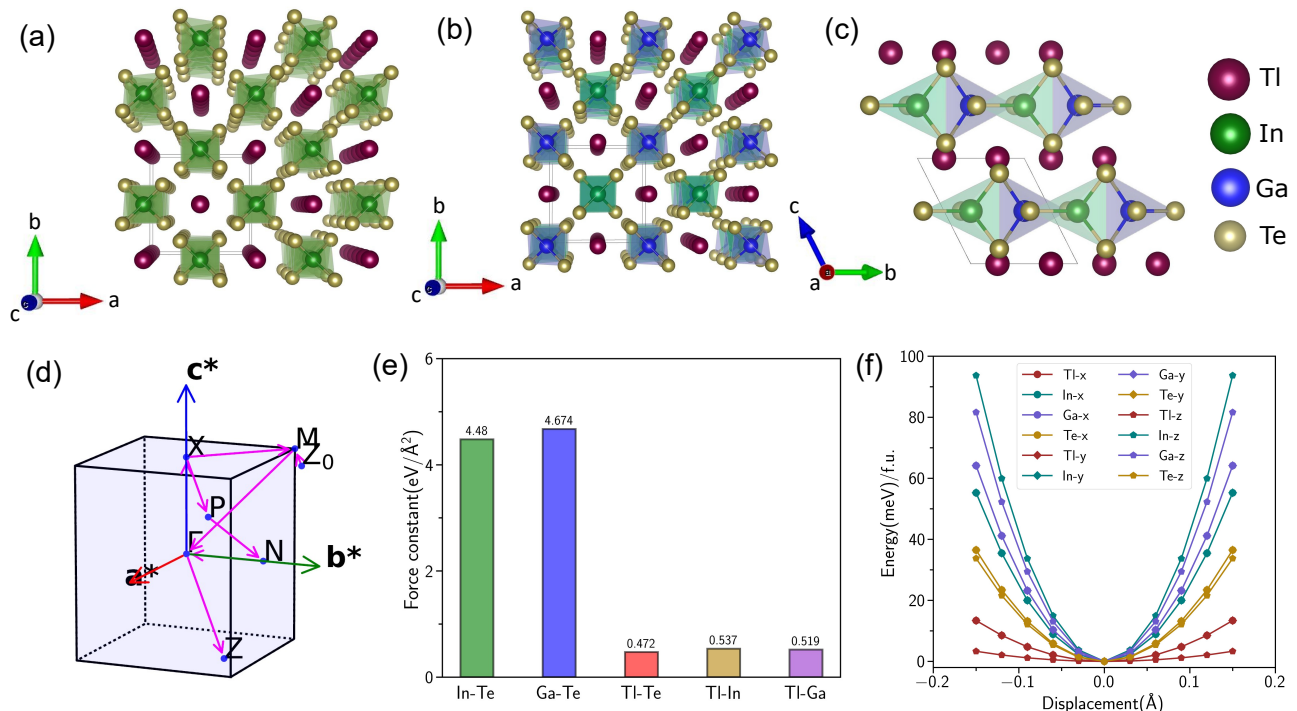


FIG. 2. Conventional crystal structure of (a) TlInTe_2 and (b) $\text{TlIn}_{0.5}\text{Ga}_{0.5}\text{Te}_2$, viewed along crystallographic c -axis. The crystal structures show a one-dimensional tetrahedral chain extended along the c -axis. (c) Primitive crystal structure of $\text{TlIn}_{0.5}\text{Ga}_{0.5}\text{Te}_2$, viewed along crystallographic a -axis. (d) The first Brillouin zone of these compounds in the k -space. (e) Second order interatomic force constants (IFC) between the atom pairs. (f) The potential energy surface (PES) of all atoms along x , y , and z -directions.

where \mathcal{V} is the volume of the primitive cell, N_c is the number of phonon eigenvectors, \mathbf{q} and s are wavevector and branch index respectively, $\bar{N}^T(q)_s$ is the Bose-Einstein distribution at temperature T , and $\Gamma(\mathbf{q})_s$ is the phonon linewidth, which is inverse proportional to the phonon lifetime ($\Gamma(\mathbf{q})_s = \Gamma_\lambda = 1/\tau_\lambda$).

III. RESULTS AND DISCUSSION

TlInTe_2 crystallizes in a tetragonal body-centered crystal structure with a space group of $I4/mcm$ (FIG. 2a). In this compound Tl, In and Te atoms adopt the oxidation states of +1, +3, and -2, respectively. The structural framework is built from In^{3+} cations tetrahedrally coordinated by Te^{2-} anions, which form $[\text{InTe}_4]^-$ covalently bonded anionic sublattice. These $[\text{InTe}_4]^-$ tetrahedra share edges with neighbouring units and give rise to one-dimensional chains extending along the crystallographic c -axis, but they are weakly connected in the crystallographic ab -plane, with no direct covalent bonding between adjacent chains. The Tl^+ ions occupy the interstitial regions between these chains and interact ionically with the $[\text{InTe}_4]^-$ framework.[35, 36]

FIG. 2b and 2c represent the conventional and primitive structures of $\text{TlIn}_{0.5}\text{Ga}_{0.5}\text{Te}_2$, respectively, where one In atom is replaced by Ga atom. In this structure, each one-dimensional chain consists of InTe_4 and GaTe_4 tetrahedra alternately (FIG. 2c). The optimized lattice parameters of TlInTe_2 are $a=b=8.41$ Å and $c=7.14$ Å,

which are in good agreement with the experimental values of $a=b=8.48$ Å and $c=7.19$ Å. In $\text{TlIn}_{0.5}\text{Ga}_{0.5}\text{Te}_2$, the lattice parameters are reduced to $a=b=8.38$ Å and $c=6.96$ Å which is attributed to the smaller size of Ga compared to In atoms. Both compounds exhibit semiconducting behaviour, as evidenced by the electronic band structures shown in FIG. S1, Supplemental Material.

To understand the bonding environment of $\text{TlIn}_{0.5}\text{Ga}_{0.5}\text{Te}_2$, we analyzed the second order interatomic force constants (IFC) and potential energy surface (PES) of all atoms (FIG. 2e and 2f). As shown in Fig. 2e, the IFC values for In-Te and Ga-Te bonds are 4.48 and 4.67 eV/Å², respectively, which are significantly larger than those involving Tl (Tl-Te, Tl-In, and Tl-Ga). This indicates In-Te and Ga-Te bonds are strong and towards covalent in nature, while Tl atoms interact weakly with the surrounding $[\text{InTe}_4]^-$ and $[\text{GaTe}_4]^-$ anionic sublattices, consistent with ionic interactions. Further, we observe the IFC between Ga-Te is slightly higher compared to In-Te, which is due to the shorter distance between Ga and Te atoms (2.67 Å) than the In and Te atoms (2.81 Å). The potential energy surface profiles in Fig. 2f further support this picture. We observe that In and Ga have a deep PES and Tl has a shallow PES, indicating In and Ga are very strongly bonded with the lattice, but Tl atoms are very loosely bonded with the lattice. This confirms that Tl atoms can vibrate with a large amplitude in the lattice, confirming the rattling nature of Tl atoms. On a closer examination, we observe that the PES of

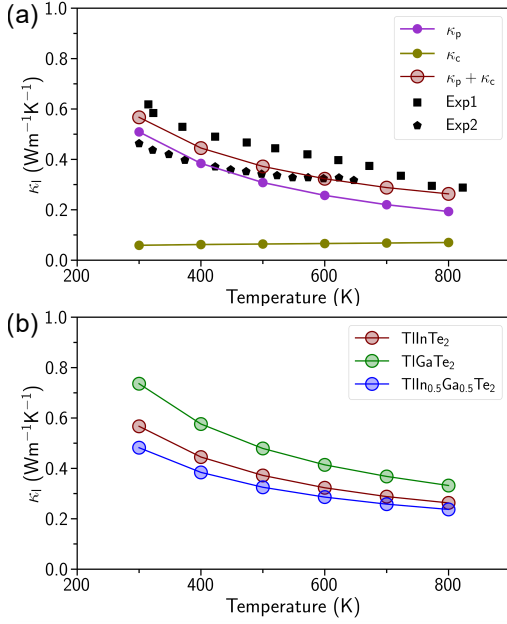


FIG. 3. (a) Temperature dependence of the calculated average population conductivity (κ_p), coherence conductivity (κ_c), and their summation ($\kappa_l = \kappa_p + \kappa_c$) of TlInTe₂ using LWTE and compared with previously experimentally reported κ_l data from Exp1[35] and Exp2[51]. (b) Temperature-dependent κ_l of TlIn_{0.5}Ga_{0.5}Te₂ and compared with TlInTe₂ and TlGaTe₂.

In and Ga along the z -axis is slightly deeper than x - and y -axes. This anisotropy arises from the strong one-dimensional tetrahedral chains extending along the crystallographic c -axis, whereas interactions along the a - and b -axes are comparatively weaker. The PES of Te atoms lies intermediate between those of In/Ga and Tl, indicating that Te atoms are less strongly bound within the one-dimensional chain compared to In and Ga, but more strongly bound than the loosely confined Tl atoms. From the anisotropy in the PES, we can expect a similar anisotropy in the lattice thermal conductivity (κ_l) in TlIn_{0.5}Ga_{0.5}Te₂.

FIG. 3a represents the temperature-dependent average population conductivity (κ_p) arising from particle-like phonon propagation, coherence conductivity (κ_c) due to wave-like phonon tunnelling, and total lattice thermal conductivity ($\kappa_l = \kappa_p + \kappa_c$) of TlInTe₂, calculated using LWTE and compared with the available experimental κ_l data. κ_p arises from the diagonal elements of the heat-flux operator, which represents heat transport mediated by the propagation of phonon modes. κ_p decreases with temperature with $1/T$, following the BTE model due to the enhanced phonon-phonon scattering at the higher temperatures. On the other hand, κ_c comes from the off-diagonal elements of the heat-flux operator, which describes the wave-like tunnelling of thermal energy due to the coupling between quasi-degenerate phonon modes. With increasing temperature, enhanced phonon-phonon scattering leads to a broadening of phonon linewidths, which creates stronger coupling between quasi-degenerate phonon modes. As a result, κ_c

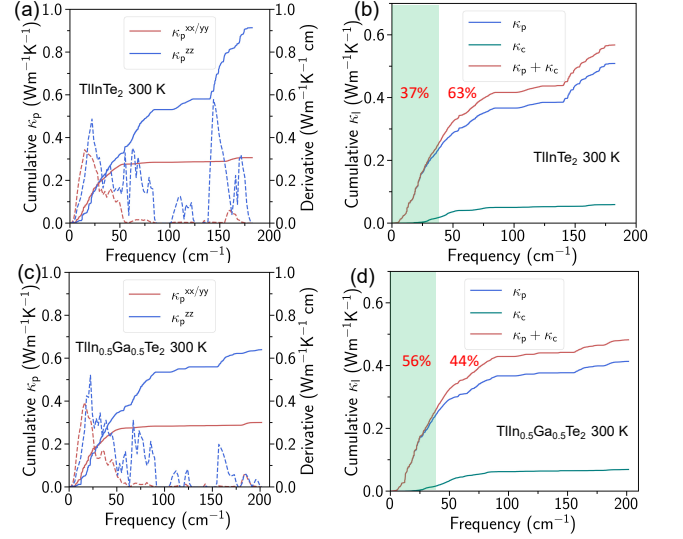


FIG. 4. Cumulative κ_p as a function of phonon frequency and its derivative of (a) TlInTe₂ and (c) TlIn_{0.5}Ga_{0.5}Te₂ along xx/yy and zz -direction at 300 K. Average cumulative κ_p , κ_c , and $\kappa_l = \kappa_p + \kappa_c$ of (b) TlInTe₂ and (d) TlIn_{0.5}Ga_{0.5}Te₂ at 300 K. Green and white regions of (c) and (d) indicate acoustic and optical regions, respectively.

exhibits a slight increase with temperature. In TlInTe₂ κ_p decreases from 0.509 Wm⁻¹K⁻¹ at 300 K to 0.193 Wm⁻¹K⁻¹ at 800 K, whereas κ_c shows a slight increase from 0.059 Wm⁻¹K⁻¹ to 0.070 Wm⁻¹K⁻¹ over the same temperature range. Thus, the κ_l of TlInTe₂ is predominantly governed by κ_p , and the contribution of κ_c is negligible. The total κ_l decreases from 0.568 Wm⁻¹K⁻¹ at 300 K to 0.263 Wm⁻¹K⁻¹ at 800 K. The calculated κ_l values are in good agreement with previously reported experimental data by Matsumoto et al.[51] and Jana et al.,[35], which validates the reliability of our present theoretical calculations (FIG. 3a). Further we applied boundary scattering, which scatters the long-wavelength phonons and plays a significant role in limiting the κ_l at the lower temperatures. With boundary scattering of 30 nm grain boundary size, the calculated κ_l reproduces the experimental data of Jana et al.[35] more accurately at low temperatures (FIG. S3, Supplemental Material). Pal et al.[36] showed that κ_l using LWTE coupled with phonon frequency renormalization at finite temperatures using the self-consistent phonon (SCPH) method[52] also reproduces the experimental data of Matsumoto et al.[51]. The low κ_l in TlInTe₂ is attributed to the bonding heterogeneity and rattling of Tl atoms, which scatters the heat-carrying acoustic phonons significantly and reduce the sound velocity of the system.

When all the In atoms are replaced by Ga atoms, the κ_l of TlGaTe₂ has increased to 0.736 Wm⁻¹K⁻¹ at 300 K due to lighter Ga atoms compared to In atoms (FIG. 3b). The calculated κ_l of TlGaTe₂ is also in good agreement with available experimental data (FIG. S4, Supplemental Material). However, when 50% of In atoms of TlInTe₂ is replaced by Ga atoms, the κ_l of TlIn_{0.5}Ga_{0.5}Te₂ is decreased to 0.482 Wm⁻¹K⁻¹ at 300 K (FIG. 3b). De-

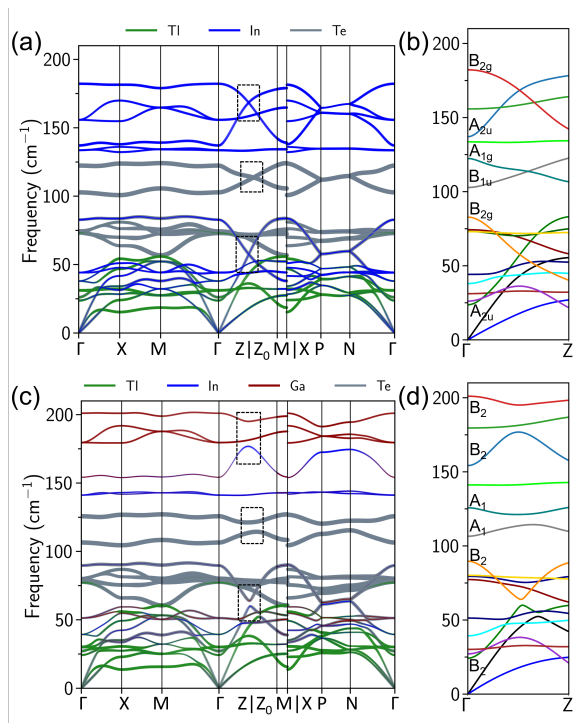


FIG. 5. Atom-projected phonon dispersion of (a) TlInTe_2 and (c) $\text{TlIn}_{0.5}\text{Ga}_{0.5}\text{Te}_2$. The phonon crossing points in TlInTe_2 , which which evolve into avoided crossing in $\text{TlIn}_{0.5}\text{Ga}_{0.5}\text{Te}_2$ along Γ -Z direction, are highlighted by dotted black boxes. Enlarged view of the Γ -Z direction of the phonon dispersion are shown in (b) and (d) for TlInTe_2 and $\text{TlIn}_{0.5}\text{Ga}_{0.5}\text{Te}_2$, respectively. The irreducible representations of the phonon modes at the Γ point corresponding to the crossing and avoided-crossing branches are also indicated.

spite the lighter mass of Ga, this reduction indicates that the decrease in κ_l is not governed by mass effects, but is instead driven by modifications in phonon dispersion. FIG. S5, Supplemental Material shows the components of κ_p and κ_c along xx/yy and zz -directions of $\text{TlIn}_{0.5}\text{Ga}_{0.5}\text{Te}_2$. It is observed that both κ_p and κ_c are higher along the z -direction, with the anisotropy being more pronounced for κ_p . Thus the κ_l is significantly higher along z -direction ($0.745 \text{ Wm}^{-1}\text{K}^{-1}$ at 300 K) than xx/yy -directions ($0.351 \text{ Wm}^{-1}\text{K}^{-1}$ at 300 K). This anisotropic behavior originates from the one-dimensional tetrahedral chain along the crystallographic c -axis, which allows better heat transport along zz -direction, while the weaker interchain interactions limit heat conduction in the ab -plane.

To understand the specific phonon contribution in the κ_l , we have plotted cumulative κ_l as a function of frequency of TlInTe_2 and $\text{TlIn}_{0.5}\text{Ga}_{0.5}\text{Te}_2$ at 300 K, as shown in FIG. 4. The cumulative κ_p with frequency along xx/yy and zz -directions of TlInTe_2 shows that along the xx/yy -direction maximum amount of κ_p is contributed by the acoustic region ($\sim 61\%$), whereas the contribution of optical region is less ($\sim 29\%$). However, along the zz -direction, an opposite trend is observed. In this direction, only $\sim 23\%$ of κ_p is originates from the acoustic region and $\sim 77\%$ of κ_p is contributed by optical re-

gion (FIG. 4a). After adding κ_c with κ_p , the total κ_l comprises approximately 37% acoustic and 63% optical contributions (Green and white regions is FIG. 4b indicates acoustic and optical regions, respectively). Interestingly, along the zz -direction, we observe a sharp jump in cumulative κ_p at $\sim 150 \text{ cm}^{-1}$, which indicates the optical phonons around this frequency range plays an important contribution in the κ_l (FIG. 4a). This is further highlighted by a sharp peak in the derivative of the cumulative κ_p along zz -direction at $\sim 150 \text{ cm}^{-1}$. We observe that this sharp peak is higher than the peak in the acoustic region (FIG. 4a). These results confirm that the thermal transport of TlInTe_2 is dominated by optical phonons. In TlGaTe_2 , similar optical phonon dominated κ_l nature is observed, as shown in FIG. S7, Supplemental Material.

In $\text{TlIn}_{0.5}\text{Ga}_{0.5}\text{Te}_2$, the cumulative κ_p with frequency shows similar trend along the xx/yy -direction, however a pronounced suppression is observed along the zz -direction (FIG. 4c). In particular, the sharp peak in the derivative of cumulative κ_p at $\sim 150 \text{ cm}^{-1}$ in TlInTe_2 shifts to $\sim 160 \text{ cm}^{-1}$ with a significantly reduced value in $\text{TlIn}_{0.5}\text{Ga}_{0.5}\text{Te}_2$. Consequently, the optical phonon contribution in κ_p along the zz -direction is reduced to $\sim 64\%$ in $\text{TlIn}_{0.5}\text{Ga}_{0.5}\text{Te}_2$ from $\sim 77\%$ in TlInTe_2 . Thus, the overall optical phonon contribution in κ_l is reduced to $\sim 44\%$ (white region of FIG. 4d). The suppression of optical phonon contribution is further evident from the absolute values. At 300 K, the acoustic and optical contributions in κ_l for TlInTe_2 are $0.210 \text{ Wm}^{-1}\text{K}^{-1}$ and $0.358 \text{ Wm}^{-1}\text{K}^{-1}$, respectively, whereas in $\text{TlIn}_{0.5}\text{Ga}_{0.5}\text{Te}_2$, those values are $0.269 \text{ Wm}^{-1}\text{K}^{-1}$ and $0.213 \text{ Wm}^{-1}\text{K}^{-1}$. Thus, these results clearly demonstrates that optical phonons are responsible in suppressing the κ_l in the partial Ga-substituted TlInTe_2 .

To elucidate the role of specific optical phonon modes in lowering the κ_l of $\text{TlIn}_{0.5}\text{Ga}_{0.5}\text{Te}_2$, we have calculated atom projected phonon dispersion of both compounds, as shown in FIG. 5a and 5c. FIG. 5a shows that in TlInTe_2 the low frequency optical modes are dominated by Tl atoms, whereas mid and high frequency optical modes are contributed by In and Te atoms. On a closer inspection of the phonon dispersion of TlInTe_2 , few interesting features are observed. We find several highly dispersive optical phonon modes along the Γ -Z, X-P and N- Γ directions. These highly dispersive modes are mainly associated with In atoms, while the Te-dominated modes are comparatively less dispersive. Interestingly, several phonon branch crossings between the optical phonon branches are observed along the Γ -Z direction, highlighted by dotted black boxes in Fig. 5a. To examine these crossings more clearly, an enlarged view of the Γ -Z direction is shown in Fig. 5b. In addition, phonon branch connectivity was analyzed using the eigenvector overlap, implemented in phonopy code, [43, 44] which is defined as

$$S_{\lambda\lambda'}(q, q + \Delta q) = |\langle e_{\lambda}(q) | e_{\lambda'}(q + \Delta q) \rangle|, \quad (5)$$

where $e_{\lambda}(q)$ is phonon eigen vector at λ mode at q point. Using this equation, the overlap between eigenvectors of two adjacent points are calculated and the eigenvectors with highest overlap are considered most similar, so

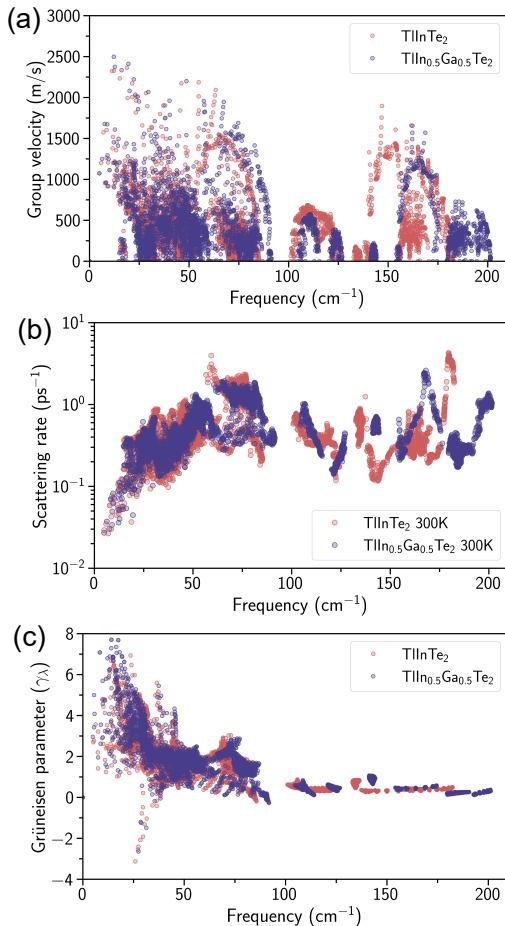


FIG. 6. Comparison of frequency-dependent (a) phonon group velocity (v_g), (b) scattering rate, and (c) Grüneisen parameter (γ_λ) of TlInTe₂ and TlIn_{0.5}Ga_{0.5}Te₂.

they are assumed to belong to same phonon branch. We have used different colours to separate different phonon branches. FIG. 5b shows that along Γ -Z direction, the bands corresponds to the black dot box in FIG. 5a are clearly crossing. We also calculated irreducible representation at the Γ point of the phonon branches participated in crossing each other. The irreducible representation shows that the phonon branches belongs to different symmetry representations ((A_{2u}, B_{2g}), (B_{1u}, A_{1g}), and (A_{2u}, B_{2g})) are crossing, which proves that phonon modes belonging to different symmetry groups are non-interacting and they cross each other without hybridization. TlGaTe₂ also exhibits similar phonon branch crossing along Γ -Z point, as shown in FIG. S8, Supplemental Material.

The atom-projected phonon dispersion of TlIn_{0.5}Ga_{0.5}Te₂ (FIG. 5c) shows an increased maximum phonon frequency compared to TlInTe₂ and high-frequency range is mainly dominated by Ga due to its lower mass than In atoms. Surprisingly, the phonon branches that intersect in TlInTe₂ evolve into avoided crossings in TlIn_{0.5}Ga_{0.5}Te₂ as highlighted by the dotted black boxes in FIG. 5c. The enlarged view of phonon dispersion along Γ -Z direction in FIG. 5d clearly shows

TABLE I. Mode-average phonon group velocity (\bar{v}), relaxation time ($\bar{\tau}$) at 300 K, and Grüneisen parameter ($\bar{\gamma}$) of TlInTe₂ and TlIn_{0.5}Ga_{0.5}Te₂.

Parameter	TlInTe ₂	TlIn _{0.5} Ga _{0.5} Te ₂
\bar{v}_g (m/s)	704.20	638.56
$\bar{\tau}$ (ps)	4.04	3.90
$\bar{\gamma}$	1.56	1.59

the repulsion between the interacting phonon branches. Additionally, the irreducible representation at Γ point shows same symmetry corresponding to the interacting branches, which are (B₂,B₂), (A₁,A₁), and (B₂,B₂). This symmetry modification in the phonon modes is associated with the partial Ga doping in pristine TlInTe₂. Thus, the phonon modes with same symmetry no longer intersect; instead, they hybridize and repel each other, giving rise to characteristic gap opening at the crossing points.

The emergence of avoided crossings among optical phonon branches leads to a flattening of the optical phonon dispersion, resulting in a reduction of the corresponding phonon group velocity (v_g). As shown in Fig. 6(a), the optical phonon v_g in TlIn_{0.5}Ga_{0.5}Te₂ is noticeably suppressed compared to TlInTe₂, particularly within the frequency ranges 100-125 cm⁻¹ and 150-200 cm⁻¹, which coincide with the avoided-crossing regions. The phonon-phonon scattering rate and Grüneisen parameter (γ_λ) vs frequency plot for TlInTe₂ and TlIn_{0.5}Ga_{0.5}Te₂ are shown in FIG. 6b and 6c. For better comparison, we have calculated mode average v_g , lifetime (τ), and γ for both compounds using the equations:[34]

$$\bar{v}_g = \sqrt{\frac{\sum_\lambda C_{V\lambda} v_\lambda^2 \tau_\lambda}{\sum_\lambda C_{V\lambda} \tau_\lambda}}, \quad (6)$$

$$\bar{\tau} = \frac{\sum_\lambda C_{V\lambda} v_\lambda^2 \tau_\lambda}{\sum_\lambda C_{V\lambda} v_\lambda^2}, \quad (7)$$

$$\bar{\gamma} = \frac{\sum_\lambda |\gamma_\lambda| C_{V\lambda}}{\sum_\lambda C_{V\lambda}}, \quad (8)$$

where C_V is phonon specific heat and λ is phonon mode. The calculated values are summarized in Table I. We observe that \bar{v}_g is strongly reduced in TlIn_{0.5}Ga_{0.5}Te₂, which is associated with the emergence of avoided crossings between the optical phonon branches. The higher $\bar{\gamma}$ also increases phonon-scattering rate slightly in TlIn_{0.5}Ga_{0.5}Te₂ and reduces $\bar{\tau}$. As $\kappa_p = \sum_\lambda C_{V\lambda} v_\lambda^2 \tau_\lambda$ within the phonon gas model under the single-mode approximation (SMA) method, the larger reduction in \bar{v}_g indicates that the lower κ_l in TlIn_{0.5}Ga_{0.5}Te₂ is primarily governed by reduced v_g , while enhanced anharmonic scattering provides an additional contribution in suppressing κ_l .

Further, we have compared the mode-resolved phonon mean free path (Λ) of TlInTe₂ and TlIn_{0.5}Ga_{0.5}Te₂ at 300

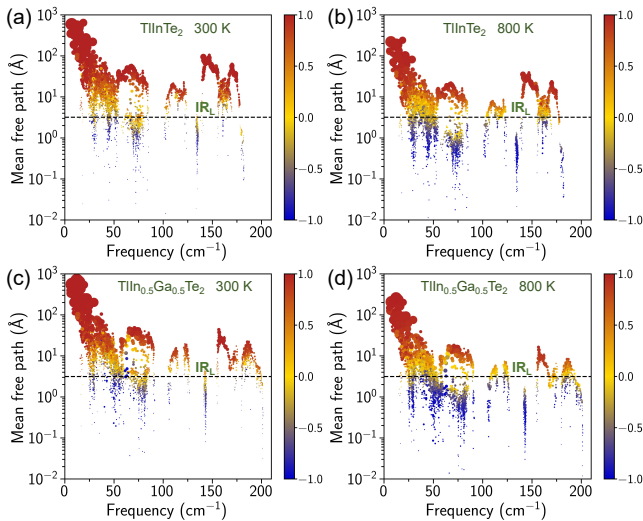


FIG. 7. Phonon mean free path (Λ) as a function of phonon frequency of TlInTe_2 at (a) 300 K, and (b) 800 K. Λ as a function of phonon frequency of $\text{TlIn}_{0.5}\text{Ga}_{0.5}\text{Te}_2$ at (c) 300 K, and (d) 800 K.

K and 800 K, as shown FIG. 7. Here, the area of each circle is proportional to the ratio of thermal conductivity of that mode ($\kappa_p(\mathbf{q})_s + \kappa_c(\mathbf{q})_s$) to total lattice thermal conductivity (κ_l) of the system. Thus, the size of each circle represents the relative contribution of an individual phonon mode to heat transport. The colour of each circle represents the quantity $c = \frac{\kappa_p(\mathbf{q})_s - \kappa_c(\mathbf{q})_s}{\kappa_p(\mathbf{q})_s + \kappa_c(\mathbf{q})_s}$, which characterizes the degree of particle-like and wave-like nature of a phonon mode. So, the brown region ($c = +1$) corresponds to purely particle-like phonon transport, whereas the blue region ($c = -1$) indicates wave-like phonon coherence. The intermediate yellow region represents the coexistence of both particle-like and wave-like transport characteristics. The dashed line represents the ‘‘Ioffe-Regel limit’’ (IR_L), which sets a threshold limit so that phonon modes above IR_L are considered as propagating modes, whereas modes below it are regarded as non-propagating or localized vibrations.[53–55] IR_L is approximated as average interatomic distance of a system.[47] For TlInTe_2 and $\text{TlIn}_{0.5}\text{Ga}_{0.5}\text{Te}_2$, the calculated IR_L are 3.19 Å and 3.14 Å, respectively. At 300 K, most of the phonon modes are found above IR_L and participated in κ_p in both systems. With increasing temperature 300 K to 800 K, Λ decrease significantly due to higher phonon scattering at higher temperature, causing a larger number of phonon modes to cross the IR_L , and consequently the contribution of wave-like phonon coherence increases. More importantly, we observe that the Λ of phonon modes between 150–200 cm^{-1} in $\text{TlIn}_{0.5}\text{Ga}_{0.5}\text{Te}_2$ is lower than that those of TlInTe_2 . In addition, the relative thermal conductivity contribution of these modes, rep-

resented by the circle size, is significantly suppressed in $\text{TlIn}_{0.5}\text{Ga}_{0.5}\text{Te}_2$ compared to the acoustic phonon modes. This results further confirm that avoided crossings at the optical phonon suppress the phonon transport and leads to reduce κ_l in $\text{TlIn}_{0.5}\text{Ga}_{0.5}\text{Te}_2$.

IV. CONCLUSION

In this work, we demonstrated that optical-optical avoided crossings provide an effective mechanism for suppressing lattice thermal conductivity in $\text{TlIn}_{0.5}\text{Ga}_{0.5}\text{Te}_2$. Using the Wigner formalism of thermal transport (LWTE), we observe populations conductivity (κ_p) is the primary transport channel in these compounds. In pristine TlInTe_2 , the calculated κ_l is $0.568 \text{ Wm}^{-1}\text{K}^{-1}$ at 300 K, where optical phonons dominate the heat transport and contribute nearly 63% of κ_l . Upon 50% Ga substitution in TlInTe_2 , the κ_l of $\text{TlIn}_{0.5}\text{Ga}_{0.5}\text{Te}_2$ is reduced to $0.482 \text{ Wm}^{-1}\text{K}^{-1}$ at 300 K. This reduction in κ_l primarily comes from the optical phonon region, as shown in the cumulative κ_l vs frequency analysis. The phonon dispersion of TlInTe_2 exhibits several phonon crossing points in the optical region, which evolve into avoided crossings in $\text{TlIn}_{0.5}\text{Ga}_{0.5}\text{Te}_2$. The irreducible representation analysis at Γ -point shows that phonon branches belongs to different symmetry representations in TlInTe_2 are crossing, which modified into same symmetry representation in $\text{TlIn}_{0.5}\text{Ga}_{0.5}\text{Te}_2$. The phonon modes with same symmetry do not intersect; instead they repel each other and giving rise to characteristic gap openings at the crossing points. The avoided crossings in $\text{TlIn}_{0.5}\text{Ga}_{0.5}\text{Te}_2$ reduce phonon group velocity strongly within the frequency ranges 100–125 cm^{-1} and 150–200 cm^{-1} . and consequently the optical phonon contribution to κ_p is reduced to 44 %. Further analysis of the mode-averaged transport parameters, \bar{v}_g , $\bar{\tau}$ and $\bar{\gamma}$, reveals a significant suppression of \bar{v}_g in $\text{TlIn}_{0.5}\text{Ga}_{0.5}\text{Te}_2$, indicating that the reduction in κ_l is primarily governed by reduced phonon group velocity induced by avoided crossings at the optical region. The slightly higher $\bar{\gamma}$ and lower $\bar{\tau}$ indicates that the enhanced anharmonic scattering provides an additional contribution in lowering κ_l . Thus, our work establishes that symmetry-modified optical-optical avoided crossings can serve as an effective mechanism for reducing κ_l in compounds where optical phonons significantly contribute to heat transport.

ACKNOWLEDGMENTS

S.P. thanks CSIR, Government of India, for providing the SRF CSIR Fellowship. S.K.P. acknowledges ANRF J. C. Bose National Fellowship (File number: ANRF/SKP/4719) and ANRF, Govt. of India for funding. S.P. and S.K.P. thanks JNCASR and Param Yukti, under the National Supercomputing Mission (NSM), Government of India for providing computation facilities.

[1] G. Tan, L.-D. Zhao, and M. G. Kanatzidis, *Chem. Rev.* **116**, 12123 (2016).

[2] X. Qian, J. Zhou, and G. Chen, *Nat. Mater.* **20**, 1188 (2021).

- [3] D. Sarkar, A. Bhui, I. Maria, M. Dutta, and K. Biswas, *Chem. Soc. Rev.* **53**, 6100 (2024).
- [4] N. P. Padture, M. Gell, and E. H. Jordan, *Science* **296**, 280 (2002).
- [5] Y. Huang, Z. Deng, Y. Chen, and C. Zhang, *Appl. Energy* **335**, 120745 (2023).
- [6] M. A. Green and S. P. Bremner, *Nat. Mater.* **16**, 23 (2017).
- [7] K. Pal, Y. Xia, J. He, and C. Wolverton, *Phys. Rev. Mater.* **3**, 085402 (2019).
- [8] M. Christensen, A. B. Abrahamsen, N. B. Christensen, F. Juranyi, N. H. Andersen, K. Lefmann, J. Andreasson, C. R. Bahl, and B. B. Iversen, *Nat. Mater.* **7**, 811 (2008).
- [9] H. Lin, G. Tan, J.-N. Shen, S. Hao, L.-M. Wu, N. Calta, C. Malliakas, S. Wang, C. Uher, C. Wolverton, *et al.*, *Angew. Chem. Int. Ed.* **55**, 11431 (2016).
- [10] R. Pathak, S. Paul, S. Das, A. Das, S. K. Pati, and K. Biswas, *Angew. Chem. Int. Ed.* **63**, e202408908 (2024).
- [11] R. Pathak, S. Paul, S. Biswas, S. K. Pati, and K. Biswas, *Proc. Natl. Acad. Sci.* **123**, e2521353123 (2026).
- [12] H. Liu, X. Shi, F. Xu, L. Zhang, W. Zhang, L. Chen, Q. Li, C. Uher, T. Day, and G. J. Snyder, *Nat. Mater.* **11**, 422 (2012).
- [13] Y. Zhang, X. Ke, P. R. Kent, J. Yang, and C. Chen, *Phys. Rev. Lett.* **107**, 175503 (2011).
- [14] J. He, Y. Xia, W. Lin, K. Pal, Y. Zhu, M. G. Kanatzidis, and C. Wolverton, *Adv. Funct. Mater.* **32**, 2108532 (2022).
- [15] K. Biswas, J. He, I. D. Blum, C.-I. Wu, T. P. Hogan, D. N. Seidman, V. P. Dravid, and M. G. Kanatzidis, *Nature* **489**, 414 (2012).
- [16] Y. Pei, G. Tan, D. Feng, L. Zheng, Q. Tan, X. Xie, S. Gong, Y. Chen, J.-F. Li, J. He, *et al.*, *Adv. Energy Mater.* **7**, 1601450 (2017).
- [17] B. Jiang, Y. Yu, J. Cui, X. Liu, L. Xie, J. Liao, Q. Zhang, Y. Huang, S. Ning, B. Jia, *et al.*, *Science* **371**, 830 (2021).
- [18] A. Bhui, S. Biswas, S. Paul, S. Das, A. Ghosh, D. Swain, T. K. Maji, S. K. Pati, and K. Biswas, *J. Am. Chem. Soc.* **147**, 29542 (2025).
- [19] Y. Zheng, T. J. Slade, L. Hu, X. Y. Tan, Y. Luo, Z.-Z. Luo, J. Xu, Q. Yan, and M. G. Kanatzidis, *Chem. Soc. Rev.* **50**, 9022 (2021).
- [20] M. Beekman and D. G. Cahill, *Cryst. Res. Technol.* **52**, 1700114 (2017).
- [21] J. Duhan, C. Wolverton, and K. Pal, *Phys. Rev. Appl.* **24**, L041003 (2025).
- [22] W. Li, J. Carrete, G. K. Madsen, and N. Mingo, *Phys. Rev. B* **93**, 205203 (2016).
- [23] P. Acharyya, T. Ghosh, K. Pal, K. S. Rana, M. Dutta, D. Swain, M. Etter, A. Soni, U. V. Waghmare, and K. Biswas, *Nat. Commun.* **13**, 5053 (2022).
- [24] Z. Zeng, Z. Fan, M. Simoncelli, C. Chen, T. Liang, Y. Chen, G. Thornton, and B. Cheng, *Proc. Natl. Acad. Sci.* **122**, e2415664122 (2025).
- [25] F. Li, X. Liu, N. Ma, Y.-C. Yang, J.-P. Yin, L. Chen, and L.-M. Wu, *J. Am. Chem. Soc.* **145**, 14981 (2023).
- [26] W. Lin, J. He, X. Su, X. Zhang, Y. Xia, T. P. Bailey, C. C. Stoumpos, G. Tan, A. J. Rettie, D. Y. Chung, *et al.*, *Adv. Mater.* **33**, 2104908 (2021).
- [27] B. Sales, D. Mandrus, and R. K. Williams, *science* **272**, 1325 (1996).
- [28] M. Rull-Bravo, A. Moure, J. Fernández, and M. Martín-González, *RSC Adv.* **5**, 41653 (2015).
- [29] T. Takabatake, K. Suekuni, T. Nakayama, and E. Kaneshita, *Rev. Mod. Phys.* **86**, 669 (2014).
- [30] J. Dong, O. F. Sankey, and C. W. Myles, *Phys. Rev. Lett.* **86**, 2361 (2001).
- [31] S. Han, S. Dai, J. Ma, Q. Ren, C. Hu, Z. Gao, M. Duc Le, D. Sheptyakov, P. Miao, S. Torii, *et al.*, *Nat. Phys.* **19**, 1649 (2023).
- [32] W. Li and N. Mingo, *Phys. Rev. B* **91**, 144304 (2015).
- [33] R. Guo, X. Wang, Y. Kuang, and B. Huang, *Phys. Rev. B* **92**, 115202 (2015).
- [34] Z. Li, H. Xie, S. Hao, Y. Xia, X. Su, M. G. Kanatzidis, C. Wolverton, and X. Tang, *Phys. Rev. B* **104**, 245209 (2021).
- [35] M. K. Jana, K. Pal, A. Warankar, P. Mandal, U. V. Waghmare, and K. Biswas, *J. Am. Chem. Soc.* **139**, 4350 (2017).
- [36] K. Pal, Y. Xia, and C. Wolverton, *npj Comput. Mater.* **7**, 5 (2021).
- [37] G. Kresse and J. Furthmüller, *Comput. Mater. Sci.* **6**, 15 (1996).
- [38] G. Kresse and J. Furthmüller, *Phys. Rev. B* **54**, 11169 (1996).
- [39] G. Kresse and D. Joubert, *Phys. Rev. B* **59**, 1758 (1999).
- [40] P. E. Blöchl, *Phys. Rev. B* **50**, 17953 (1994).
- [41] J. P. Perdew, K. Burke, and M. Ernzerhof, *Phys. Rev. Lett.* **77**, 3865 (1996).
- [42] J. P. Perdew, A. Ruzsinszky, G. I. Csonka, O. A. Vydrov, G. E. Scuseria, L. A. Constantin, X. Zhou, and K. Burke, *Phys. Rev. Lett.* **100**, 136406 (2008).
- [43] A. Togo, *J. Phys. Soc. Jpn.* **92**, 012001 (2023).
- [44] A. Togo, L. Chaput, T. Tadano, and I. Tanaka, *J. Phys. Condens. Matter.* **35**, 353001 (2023).
- [45] A. Togo, L. Chaput, and I. Tanaka, *Phys. Rev. B* **91**, 094306 (2015).
- [46] M. Simoncelli, N. Marzari, and F. Mauri, *Nat. Phys.* **15**, 809 (2019).
- [47] M. Simoncelli, N. Marzari, and F. Mauri, *Phys. Rev. X* **12**, 041011 (2022).
- [48] L. Chaput, *Phys. Rev. Lett.* **110**, 265506 (2013).
- [49] P. B. Allen and J. L. Feldman, *Phys. Rev. Lett.* **62**, 645 (1989).
- [50] P. B. Allen and J. L. Feldman, *Phys. Rev. B* **48**, 12581 (1993).
- [51] H. Matsumoto, K. Kurosaki, H. Muta, and S. Yamanaka, *J. Appl. Phys.* **104**, 10.1063/1.2987471 (2008).
- [52] T. Tadano and S. Tsuneyuki, *Physical Review B* **92**, 054301 (2015).
- [53] M. T. Agne, R. Hanus, and G. J. Snyder, *Energy Environ. Sci.* **11**, 609 (2018).
- [54] Y. Luo, X. Yang, T. Feng, J. Wang, and X. Ruan, *Nat. Commun.* **11**, 2554 (2020).
- [55] S. Taraskin and S. Elliott, *Phys. Rev. B* **61**, 12031 (2000).